Effect of Coating Thickness on Microstructure, Mechanical Properties and Fracture Behaviour of Cold-Sprayed Ti6Al4V Coatings on Ti6Al4V Substrates

Adrian Wei-Yee Tan[1,2], Wen Sun[1,2], Ayan Bhowmik[1,2], Jun Yan Lek[1,4], Iulian Marinescu[1,3], Feng Li[1,3], Nay Win Khun[1,2], Zhili Dong[4], Erjia Liu[1,2,*]

[1]Rolls-Royce@NTU Corporate Lab, Nanyang Technological University, 50 Nanyang Avenue, Singapore 639798, Singapore

[2]School of Mechanical & Aerospace Engineering, Nanyang Technological University, 50 Nanyang Avenue, Singapore 639798, Singapore

[3]Advanced Technology Centre, Rolls-Royce Singapore Pte Ltd, 1 Seletar Aerospace Crescent, Singapore 797575, Singapore

[4]School of Materials Science and Engineering, Nanyang Technological University, 50 Nanyang Avenue, Singapore 639798, Singapore

Email: mejliu@ntu.edu.sg, Tel: +65-67905504

Abstract

Cold spray is a relatively new coating technology by which coatings can be produced without significant heating of the sprayed powder. This has gained attention in the aerospace industry as cold spray has the potential to restore damaged parts made of light metal alloys, like Ti6Al4V (Ti64 in short) components. Such repair requires high quality Ti64 coatings of varying coating thicknesses to fill the damages incurred in worn or corroded parts. However, the study of the effect of coating thickness for Ti64 coatings deposited on Ti64 substrates on their microstructure and mechanical properties has not been reported. In this work, high quality Ti64 coatings with different thicknesses were successfully deposited on Ti64 substrates. It was observed that the microstructure and mechanical properties such as low porosity level, high hardness and strong adhesion strength of the Ti64 coatings were maintained with increasing coating thickness, and thereby holding a great potential in repair industries. The interface bond strength was also successfully measured with a glueless tensile test. As for the flexural strength, the thinner Ti64 coatings could conform to the stress concentration point, better than the thicker coatings. The fracture characteristics of the coatings were also investigated.

Keywords: High-pressure cold spray, Ti6Al4V powder/coating/substrate, Mechanical properties, Coating thickness, Flexural strength, Fracture behaviour

1 Introduction

Repair of Ti6Al4V (Ti64) components is a great challenge for the aerospace industry. Commercial gas/jet turbine engines consist of a large number of Ti64 components, particularly in the compressor section of the engines where temperatures of up to 650 °C are experienced. Ti64 is particularly attractive due to its tremendous weight-saving properties owing to its high specific strength coupled with low density, corrosion resistance and good thermal stability (up to 400 °C) [1]. However, these Ti64 components suffer from wear and tear over the service period due to harsh environments such as friction and erosion and even bird strikes. As Ti64 components are expensive due to high cost of raw materials, it will be cost-effective to repair them and restore their functionality, instead of scarping them following damage during service period.

The repair of Ti64 components depends on the extent of damage and may require rebuild-up to several milimeters thick. Conventional material repair methods such as welding and direct laser deposition may not be suitable to restore these thicknesses. Further these techniques lead to instabilities in the components specifically along the repaired sections. For example, heat affected zones are invariably created, which induce thermal stresses due to thermal mismatch between the joining components and also result in substantial distortion of the microstructure that might involve phase changes, precipitation, etc. which may create areas of mechanical weaknesses leading to eventual failure around the actual lines of repair [2-4]. As such, cold spray may be an alternative technique to build required coating thicknesses as a low-temperature additive manufacturing process with minimum sample distortion. Cold spray is a process where particles are accelerated to supersonic speeds and impact on the target substrate surface to form a coating. The particles remain in their solid-state condition throughout the process. The detailed working principle of cold spray process has been widely reported in the literature [5-13].

Recently, cold sprayed Ti64 coatings have been widely investigated as they can be potentially used in many applications. Some works have been carried out to understand the splat deformation of cold sprayed Ti64 particles. Goldbaum et al. [14] observed that Ti64 splats deposited on a Ti64

substrate had a high flattening ratio (width/height ratio of particle) of 2.5-2.75, but demonstrated poor particle adhesion and bonded interface that was not fully continuous, with only traces of metallurgical bonding even at deposition velocities as high as 1115 m/s. Vid et al. [15] also studied the deposition of Ti64 splats on substrates such as titanium and magnesium with different ultimate tensile strength. The study showed that impact of Ti64 particles on substrates with similar strengths, such as Ti and Ti64 resulted in a higher degree of plastic deformation and formation of regions of shear instability in the impacted zone. This is due to the transformation of kinetic energy into localised heat within short time and volume, which favours adiabatic shear instability.

Li et al. [16] reported cold sprayed Ti64 coatings having a high porosity level of about 22.3%, especially between the deposited microparticles. On the other hand, Luo et al. [17] demonstrated that cold sprayed Ti64 coatings using He gas created denser coatings with only about 2.7% porosity. However, as He gas is much more expensive than N_2 gas, it is not economical to be used widely in industry. By using N_2, Luo et al. [17] also managed to further reduce porosity levels by incorporating larger stainless steel microparticles into the Ti64 powder feedstock, which created an additional shot-peening type of effect. The porosity level was thus reduced from about 15% to around 0.6%. However, for critical applications, these stainless-steel inclusions might act as stress concentration sites in the coatings and hence would be undesirable.

There are also limited works reported on the effect of cold sprayed Ti64 coating thickness on the bonding characteristics, which is crucial for repair of worn or corroded Ti64 components though effect of thickness has been studied on aluminium coatings. Xiong et al. discovered that shear adhesive bond strength of Al 7075 and 7050 cold sprayed coatings on unheated Al 7050 substrates decreased with the increase in coating thickness [18]. Moridi and co-workers [19] reported that thicker cold sprayed Al 6082 coatings on the substrates of the same material also resulted in lower bond strength. As an analogy, even in thermal spraying, thick coatings are usually accompanied by lower bond strengths [20] . Hence, the thickness effect of Ti64 coatings on substrates needs to be evaluated carefully as it plays a critical part in the integrity of the repaired components in application.

This work focuses on the investigation of cold sprayed Ti64 coatings on Ti64 substrates using N_2 gas under optimum conditions with particular focus on studying the thickness effect on the coating quality. The article first discusses the effect of growing coating thickness on the porosity level in the coating. It then subsequently reported the effects of this thickness on the mechanical properties such as hardness, interfacial bond strength, flexural strength of the Ti64 coatings. The results have then been rationalised on the analysis of fracture behaviour of the coated samples.

2 Experimental details

2.1 Materials

Cold-rolled pieces of Ti64 plates (Grade 5) (Titan Engineering, Singapore) with dimensions of 50 mm x 50 mm x 8 mm were used as the substrates. The substrates were ground and degreased sequentially prior to spraying. The powder feedstock used was plasma-atomized Ti64 ELI (Grade 23) powder comprising primarily spherical particles ranging from 15 to 45 μm in diameter (AP&C, Canada) as shown in Figure 1a and 1b. However, some satellites were also observed in the powder. The polished cross-section (Figure 1c) of the powders showed the absence of internal porosity while the etched cross-section (Figure 1d) shows that powders have a lath microstructure [21]. There are also no impurities detected using energy-dispersive spectroscopy (EDS), as reported in a previous work [22].

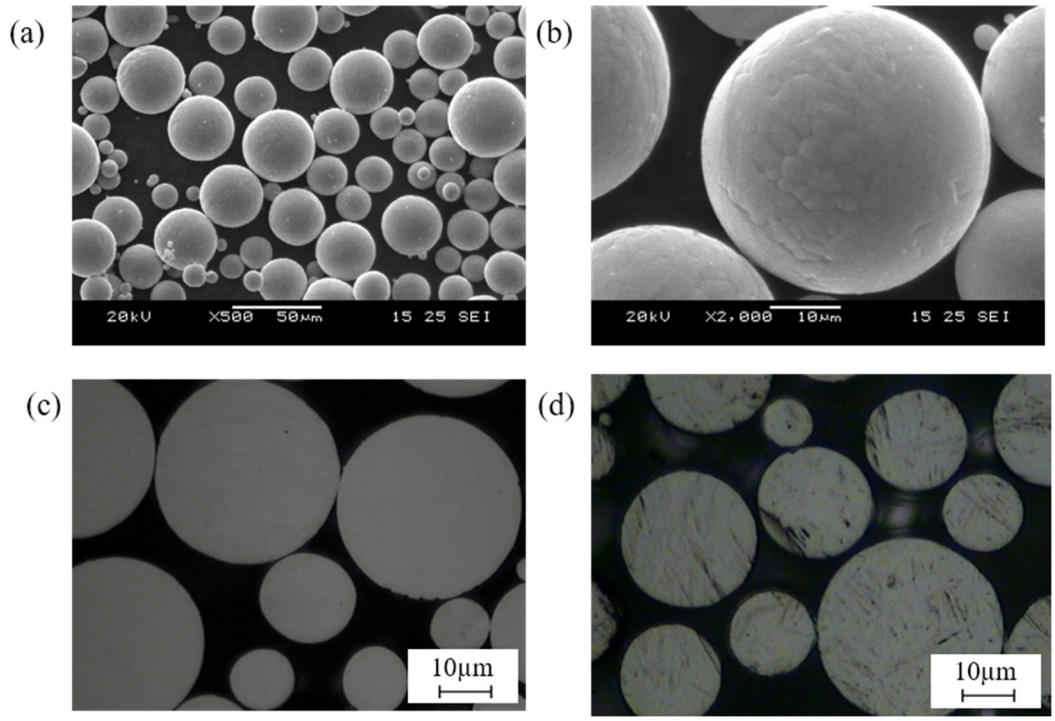

Figure 1: (a and b) SEM micrograph of pristine Ti64 powder at different magnifications, optical micrographs of (c) polished and (d) etched cross-sections of powders.

2.2 Sample preparation

An Impact Spray System 5/11 (Impact Innovations, Germany) was used to deposit the Ti64 coatings with the setup shown in previous work Figure 2a. A SiC spray nozzle of 6 mm diameter with an expansion ratio of 5.6 and a divergent section length of 160 mm was used in the spray deposition. The deposition parameters are shown in Table 1. The deposition velocity measured using Tecnar Cold Spray Meter was around 800 m/s. Prior to deposition, the substrate surfaces were heated to approximately 200 to 300°C simply by blowing preheated nitrogen gas [22] for better adhesion of the powder particles to the substrate surfaces.

Table 1: Cold spray deposition parameters

Working gas	**Gas pressure (MPa)**	**Gas temperature (°C)**	**Sample stage traverse speed (mm/s)**	**Spray angle (°)**	**Stand-off distance (mm)**	**Raster step (mm)**
Nitrogen	4.8	1100	500	90	30	1

The sample stage was rastered horizontally with a constant velocity of 500 mm/s (Figure 2b) followed by 1 mm vertical raster step after each traverse movement to form a coated layer. Each deposited layer had a thickness of ~0.15-0.17 mm, which was repeated until the desired thickness was achieved. The final thicknesses of Ti64 coatings were around 0.1 mm, 0.5 mm, 1 mm and 3 mm.

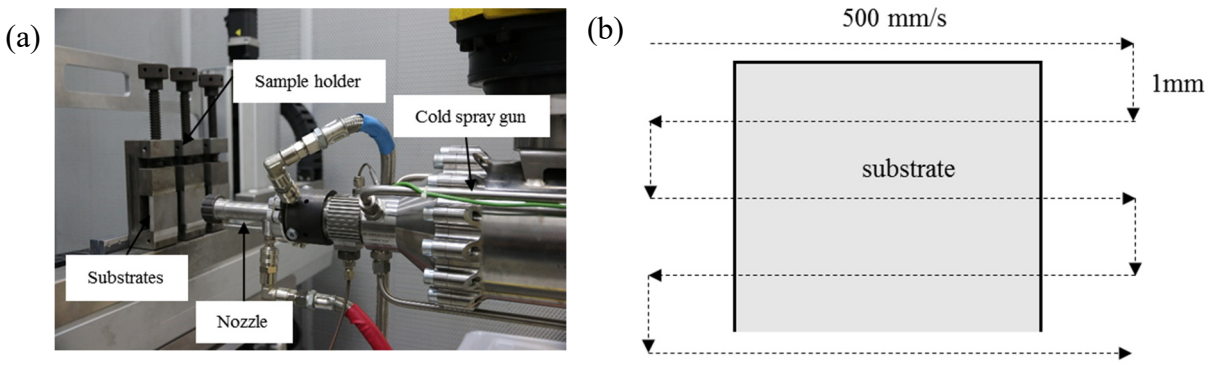

Figure 2: (a) A photograph showing the cold spray setup (referred from previous work [22] and (b) schematic of the scanning procedure showing the transverse speed of the substrate (500 mm/s) and the raster step (1 mm)

2.3 Microstructural characterisation

The surface roughness of the as-sprayed samples was measured in terms of R_a and R_z, with a contact mode surface profilometer (Talyscan 150, Taylor Hobson, USA) with a 4 µm diameter tip. The average surface roughness of each sample was calculated from three random measurements with each measurement under the conditions of scan length of 30 mm, scan step of 1 µm and scan speed of 1 mm/s.

For cross-section microstructural analysis, the cold sprayed samples were sliced into pieces with dimensions of 2 cm × 1 cm × 0.8 cm (L × W × H) each. The cut samples were then cold mounted with Specifix-20 (cured for 12 hours), ground with 320 SiC grit papers, followed by chemical-mechanical polishing (CMP) with a DiaPro solution containing 9 µm diamond particles and then an OP-S suspension solution containing 0.04 µm colloidal silica particles (Struers, Denmark). For

microstructural investigation, the polished samples were etched using Kroll's reagent by immersion method for 10 to 15 s.

Microstructures and porosities of the samples were observed under optical microscope (OM, Axioskop 2 MAT, Carl Zeiss, Germany) and/or scanning electron microscope (SEM JSM-5600LV and FESEM 7600f, JEOL, USA) operated at 15 to 30 kV. For porosity measurement, a series of 16 continuous cross section images (optical, ×200 magnification) were taken from the coating top, middle and near-interface region. These images were stitched (per location) and processed using the open source software ImageJ (NIH, USA) [21].

Elemental compositions of the samples were analysed using SEM-based Energy Dispersive Spectroscopy (EDS, Oxford Instrument, UK). Phase analysis of the cold spray samples was carried out using X-ray diffraction (XRD, Empyrean Panalytical, Netherlands) with CuK_{α} radiation operated at 40 kV acceleration voltage and 40 mA emission current, from 20 to 90° degrees of 2θ, with a dwell time of 1s for step size of 0.02°.

Transmission electron microscopy (TEM) was carried out on a foil extracted from a polished Ti64 cross-section using FEI Nova NanoLab™ 6001 focused ion beam (FIB) dual beam system. TEM was performed using a JEOL 2010 operating at 200 kV. Selected area diffractions were acquired to validate the structure of the sample.

2.4 Mechanical characterisation

Microhardnesses of the coating and substrate cross-sections of the Ti64 samples were evaluated using a Vickers microindenter (FM-300e, Future-Tech, Japan), with 300 g load and 15 s dwell time. Nanohardness measurements were also performed on the samples and powders using a nanoidenter (Agilent G200, USA) with a penetration depth of 0.5 μm. For the samples, a 5 × 5 matrix with 10 μm spacing was indented across the coating/substrate interface. As for the powders, around 15 particles with diameters around 20 to 40 μm were indented to ensure the penetration was well-confined within the particles and there were no influences from the underlying epoxy resin.

Adhesion strength test was conducted on each coated sample following the ASTM C633 standard [23]. First, the samples were wire cut into circular buttons with a diameter of 25 mm and the buttons were ground flat. Next, the top and bottom button surfaces and fixtures were sand blasted with P80 alumina particles, cleaned with ethanol and assembled together with adhesive glue (Araldite AV170, Huntsman Advanced Materials, USA). The assembled sets were then placed at a tilt angle of 35° in an oven in which the sets were cured at 150°C under a weight of 380 g for 60 min and left to cool to room temperature (~ 23 °C) . The sets were tested using a tensile tester (Instron 5569 ,UK) with a load cell of 50 kN in tensile mode with an extension rate of 0.8 mm/min till the sets failed.

A glueless method, modified from ASTM E8, was also used to measure the true coating/substrate interface bond strength. For this, a 5 mm thick Ti64 coating was deposited onto a 9 x 50 x 50 mm^3 Ti64 substrate. A flat tensile sample was fabricated by wire cutting into dimensions as shown in Figure 3a. The sample is then placed into the fixture (Figure 3b) and tested with the same Instron machine (mentioned above) but with an extension rate of 0.3 mm/s until failure.

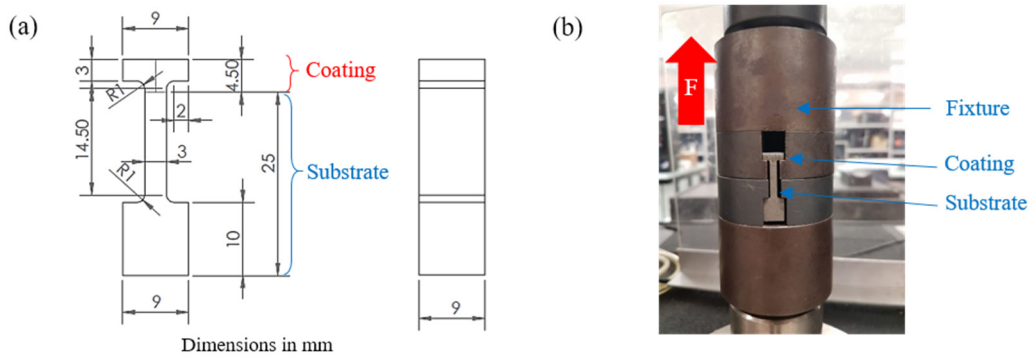

Figure 3: (a) Schematic drawing of sample for mini tensile test and (b) tensile test setup

Three-point bending tests, following ASTM E290-13 standard were conducted to investigate the flexural strength of the coating/substrate aggregate [24]. Figure 4a illustrates the schematic of test configuration and Figure 4 (b and c) show the actual setup before and after the test. The specimens used were rectangular blocks with length (l) 50 mm, width (b) 9.5-10 mm and thickness (d) 4-6.5 mm. The bending test was conducted using MTS 810 Material Testing System (USA). The span, L,

between the two supports was 40 mm and the displacement rate of the plunger (diameter, Ø = 10 mm) was 0.5 mm/min. The flexural stress, σ_f and flexural strain, ε_f were calculated with the equation: $\sigma_f = 3FL/2bd^2$ and $\varepsilon_f = 6Dd/L^2$, where F is the load at a given point on the load deflection curve (N), L is the support span (mm), b is the width of test specimen (mm), d is the thickness of tested specimen and D is the maximum deflection of the specimen at the center (mm). A test was ran on until either failure within the coating or delamination of the coating/substrate occurred. The microstructure of the fractured samples was analysed using low-magnification optical microscope (Olympus SZX7, Japan).

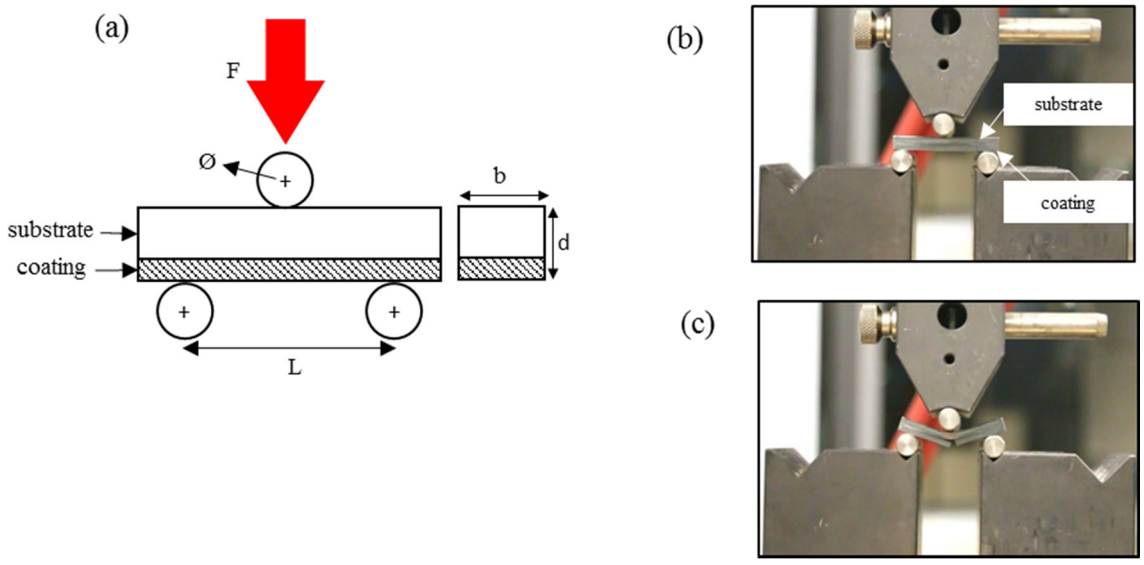

Figure 4: (a) Schematic illustration of three-point bending test, and photographs showing actual setup of (b) before and (c) after loading a sample.

3 Results and discussion

3.1 Cross-section and surface analysis

The micrographs of the polished cross-sections are shown in Figure 5(a-d) and are found that the porosity increases with coating thickness from about 2.7 to 3% (Figure 5e). All the coatings do not exhibit cracking or interface delamination (Figure 5(a-d)). The porosity distribution appears to be uniform and the interface lines are intimate. The porosity levels of the cold sprayed Ti64 coatings produced in this study were also lower than those reported in the literature, about 5 to 20%, due to lower particle impact speed from chosen deposition parameters in [16, 25-27].

The dense Ti64 coatings are attributed to the high impact energy of the sprayed particles, which causes intensive plastic deformation, thus promoting the cohesion of the particles and preventing the formation of large porosities. The dense Ti64 coatings are attributed to the high impact energy of the sprayed particles, which causes intensive plastic deformation, thus promoting the cohesion of the particles and preventing the formation of large porosities. In a cold spray deposition process, a coating is formed through several stages. At the initial stage, it is well-known that the particles are bonded to the substrate surface via the so-called adiabatic shear instability (ASI), whereby the peripheries of the incoming particles form jets and the shear stresses developed in the region result in the bonding. A major fraction of the kinetic energy of the impacting particles is converted into heat during the process within a very short time, typically in the order of a few tens of nanoseconds, of the particle collisions. The heat does not dissipate, and the impacted particles are essentially severely deformed under the adiabatic shearing conditions [28]. The subsequent stage for coating build-up consists of constant shot peening or particle hammering, which causes further plastic deformation leading to work hardening [29]. However, in this case, there is a porosity level increment from 2.7 to 3% during coating build-up from 0.1 to 3 mm. The increment of porosity level with coating thickness could be explained by the accumulation of heat during the coating build-up. As the coating surface temperature increases during the coating build-up (from 200 to 300ºC [22]), it promotes the particle adhesion where the particles travelling at lower velocities (or below critical velocities) are also able to deposit

and may result in less plastic deformation. In addition, a cold sprayed coating tends to have a higher porosity level in the top section of the coating, which is mainly due to the absence of impinging effect (or hammering effect). With the increasing coating thickness, the porosities of the top section become more prominent. Hence, these prevent complete filling of the gaps between the particles, hence slightly increasing the coating porosity level.

Another important factor is the strain rate dependent hardening of Ti64 alloys that plays an important role in hardening of the deposited splats. Ti64 has a high strain rate sensitivity with its yield strengths increasing with increasing strain rate [30]. Thus, at the strain rates encountered in cold spraying process (10^9 s^{-1}), appreciable hardening is to be expected in the Ti64 particles which make it lose its compliance and this in turn results in creation of voids. During the impact, significant heat energy is still generated upon high speed impact, but its lack of dissipation within the length scale of the particles prevents softening of the splats as it deposits. The small difference of porosity levels of 0.1%, thereon between the coating thicknesses of 0.5 mm and 3 mm indicates a steady state deposition condition for example, surface temperature, plastic strain and compaction. For example, a previous study by Tan et al. showed that temperature reaches a steady state in about 80s and considering the time for coating formation to be 17s, the temperature would have been close to steady state by 5 layers of coating, with a thickness about 0.75 mm [22].

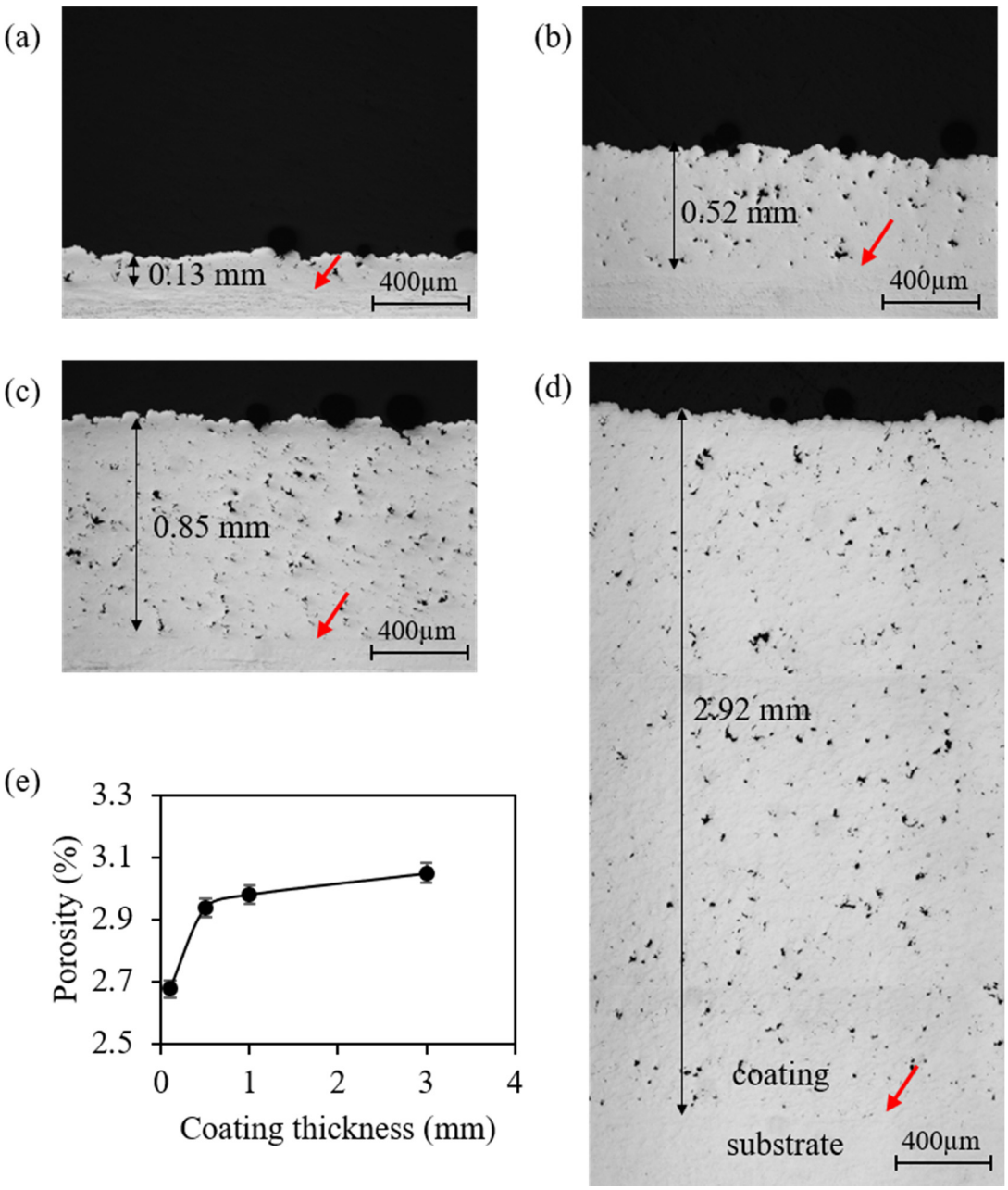

Figure 5: (a-d) Optical micrographs showing polished cross-sections of samples with coating thicknesses of around a) 0.1 mm, b) 0.5 mm, c) 1 mm and d) 3 mm, where the arrows indicate the interfaces between the coatings and substrates; (e) Plot showing average porosity levels as a function of coating thickness.

The etched cross-sections of all coatings thicknesses were observed by OM as shown in Figure 6. Due to the similarity of coating morphologies, the SEM analyses would be focused on the 3 mm coating as shown in Figure 7. The etched Ti64 coatings showed that individual impacted particles underwent severe plastic deformation with significant material jetting as the particles were impacted

above their critical velocity [14, 31], which allow ASI to occur for bonding (Figure 7) [28]. The SEM micrographs in Figure 7(a-c) also showed two distinctive contrast within varying regions of the splats – textured and smooth regions. A closer look revealed that the smooth regions correspond to the severely deformed part of the particle while the textured regions correspond to undeformed splat regions with microstructure remnant from the parent powder [21, 32]. This differential strain distribution within the splat particles would be discussed later in detail. The particle boundaries were also observed to be slightly protruded which indicates a different etch rate as compared to the textured and smooth region (Figure 7d). The boundaries may contain shear bands which consist of refined grain structures driven by severe plastic deformation which occur at the particle boundaries during impact [33-35]. Voids can also be observed at the base of the particle due to lack of shear deformations as shown in Figure 7e.

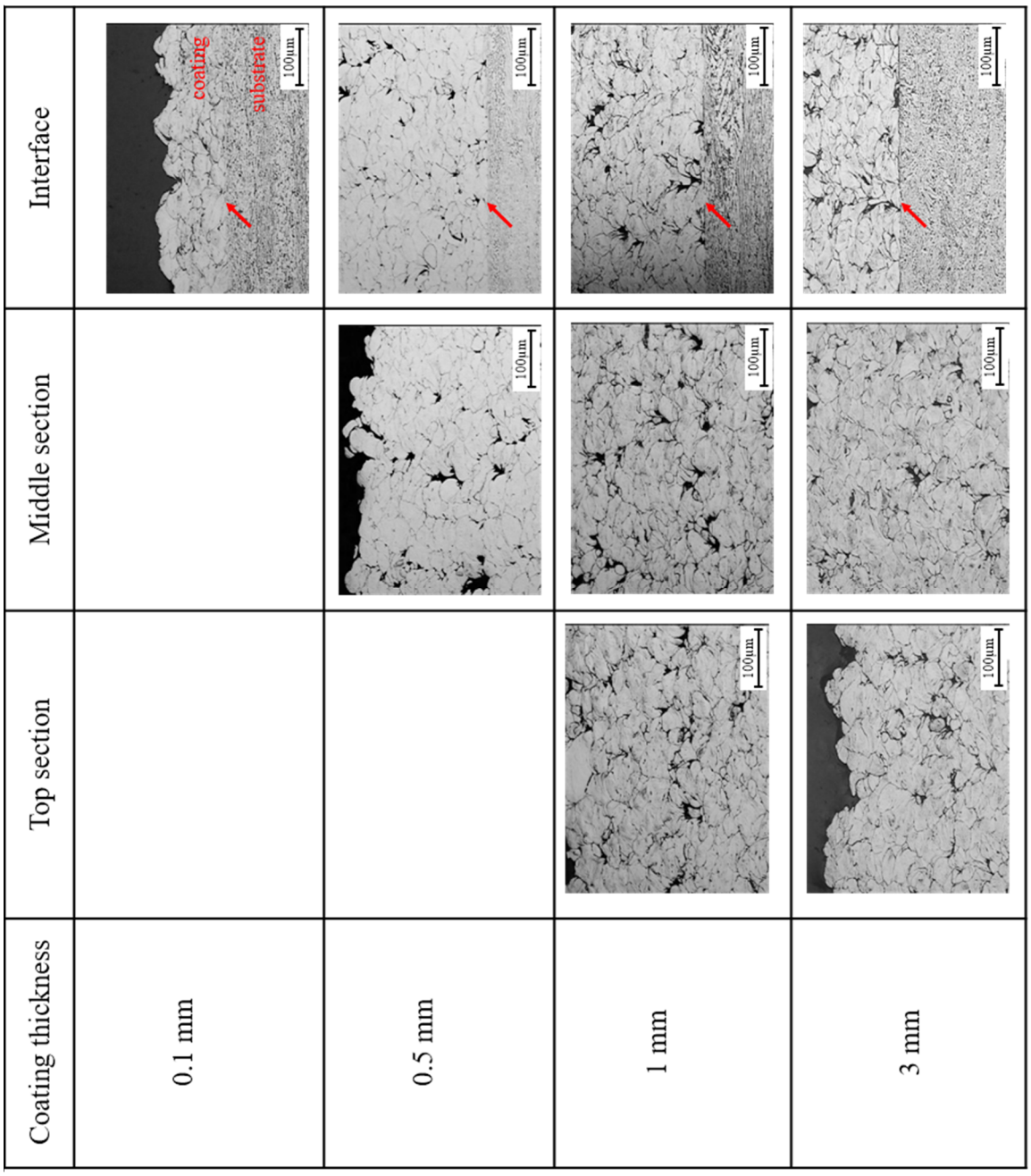

Figure 6: Optical micrographs showing microstructures of the top, middle and interface portions of the etched cross-sections of Ti64 coatings with varying coating thicknesses. The arrows indicate the interface between coating and substrate.

Figure 7f shows the agglomeration of the small (10 to 25 μm) and large (40 to 50 μm) particles in the 3 mm thick Ti64 coating. These agglomeration locations also form pores. As generally observed in the micrographs, the pores are essentially formed at the splat boundaries. It is quite evident that these pores are formed as a result of impingement of powder particles on *a priori* rough coating surface and its inability to subsequently conform around the surface asperities even under the given impact energy. The agglomeration could be a result of particle size and weight separation during the flow from the powder feeder to the nozzle exit, with a travel distance of approximately 1.2 m. The smaller and lighter particles would have travelled at higher velocities as compared to the larger and heavier particles. As such, by the time the particles reach the nozzle exit, the particles may have separated into light and heavy groups and form the coatings. Moreover during spraying from the gun, the particles follow a hump-like velocity profile along the nozzle width – the particles located at the edge of the jet travel at lower speeds compared to the particles at the center of the jet [14, 36, 37].

Such particle velocity distribution also indirectly affects the surface morphologies in terms of surface roughness. Clusters of the particles have varying degree of flattening ratio (dotted square) with inter-particle pores (dotted circle) were observed in Figure 8a. The bases of particles were also plastically deformed and underwent ASI to form material jetting (Figure 8b - solid circles), while the top section of the particles remained as semi-spherical [38]. The impact which resulted in such morphology were illustrated in Figure 8c. The surface roughness of the coatings is also found to increase with coating thickness (Figure 8d), which could be due to higher coating porosity for a thicker coating, formed at the splat boundaries.

Besides, the smaller particles have lower thermal masses with limited heat storage capability and hence exhibit lesser thermal softening as compared to the larger particles. However, the ability of limited thermal softening largely offsets the greater propensity of viscoplastic deformation of smaller particles owing to their higher velocity compared to the larger ones. Hence, it was observed that these finer particles undergo less deformation and sometimes have difficulty to fill the gaps and result in some porosities, as observed in Figure 7f in spite of the fact that smaller particles generally

are more efficient in space-filling and result in a more compact coating relative to bigger particles. Such clustering might lead to an uneven stress distribution in the coating and porosities may act as crack initiation points. Further work to improve the basic design of the spray gun nozzle in order to achieve a narrower powder distribution in the jet is required to address this issue.

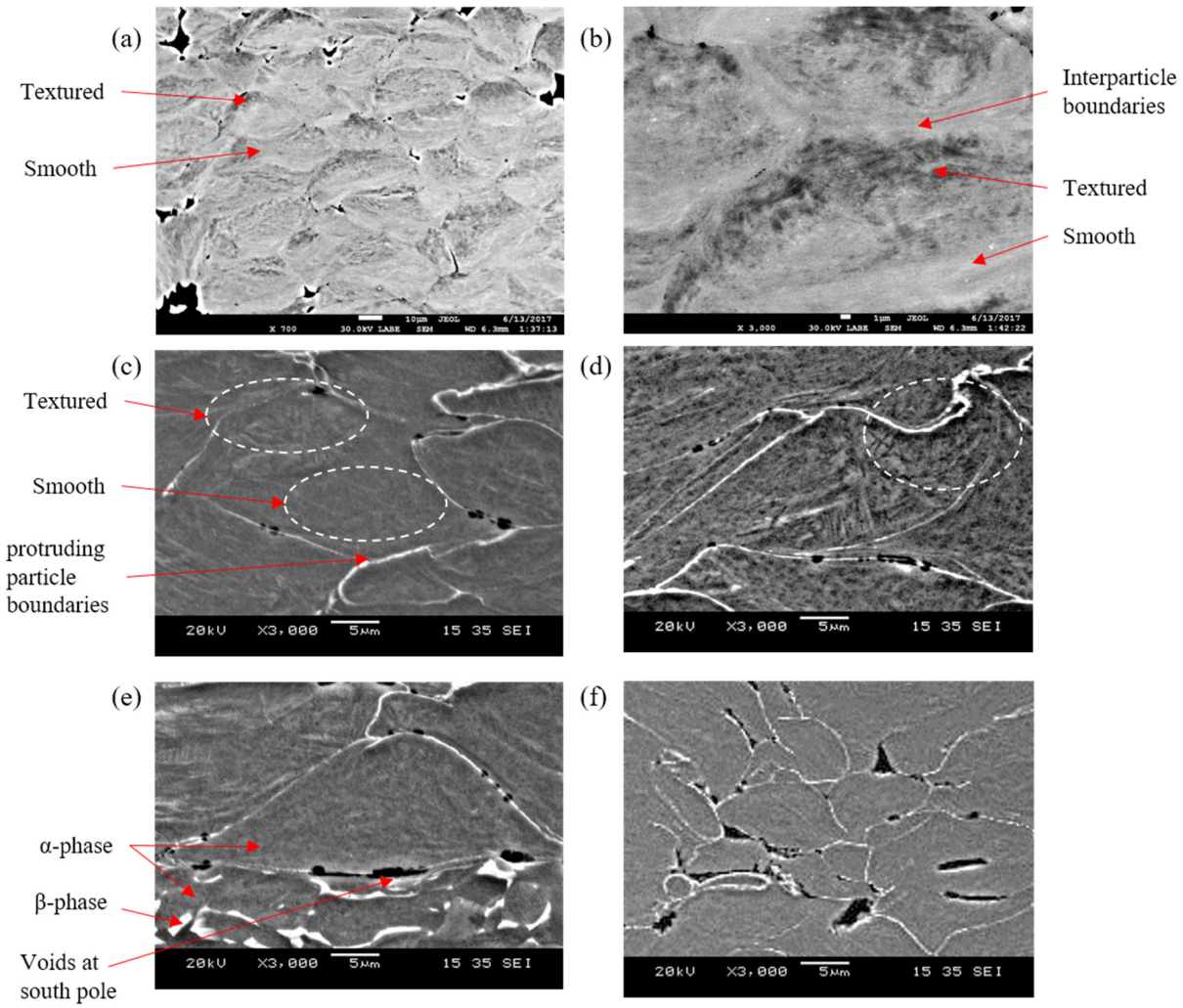

Figure 7: SEM micrographs of 3 mm thick coating: (a) Back scattered (BSE) image of cross-section, (b) higher magnification BSE image of smooth and textured region, (c) textured and smooth regions in a particle, (d) a particle with severe plastic deformation and protrusion of boundaries after etching (dotted circles), (e) deformation of a particle on the substrate and (f) agglomeration of particles.

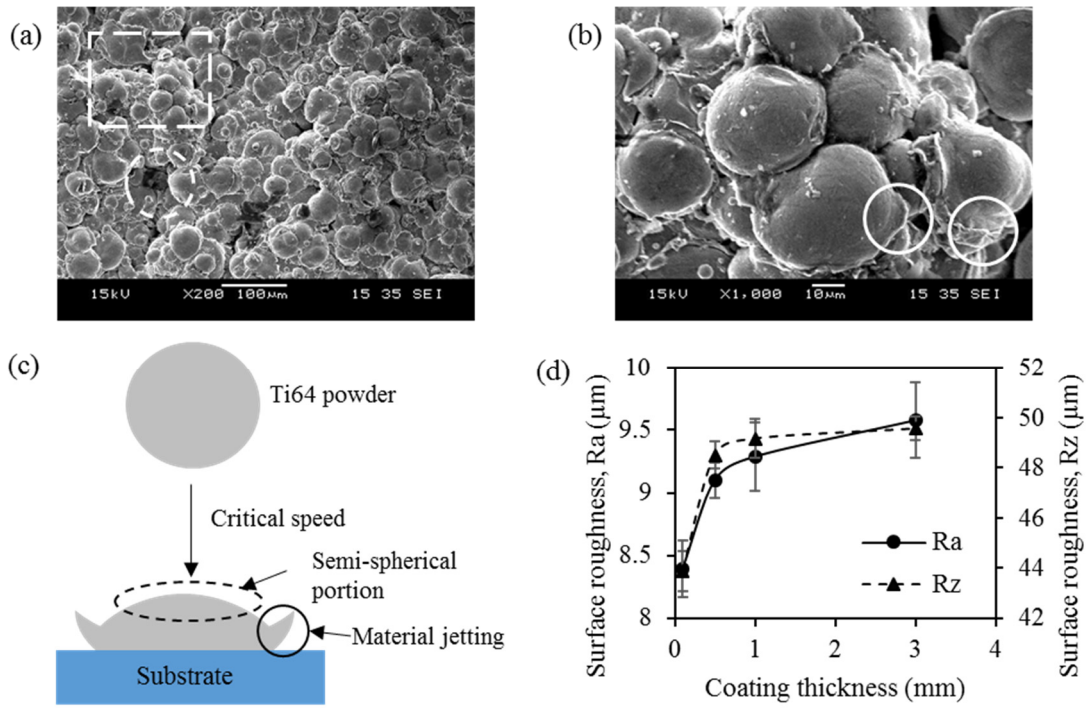

Figure 8: (a and b) SEM micrographs of as-sprayed Ti64 coating surface with different magnifications, (c) schematic illustration of microparticle jetting after impact at critical speed, and (d) surface roughness of coatings as a function of coating thickness

3.2 Phase analysis

Both XRD (Figure 9a) and EDS (Figure 9b) results show that the Ti64 (based on 1 mm thick coating) coating has no impurities or additional phases compared to the raw Ti64 powder and bare substrate. The major constituent of the Ti64 powder was HCP α-Ti phase. No reflection from the BCC β-Ti was observed in the parent powder. This can be rationalised from the fact that the powders used were synthesized by plasma atomisation whereby metal powders are condensed from the liquid droplets at a very high cooling rate, typically $>10^3$ °C/s. Thus, under such rapid solidification, it can be anticipated that the HCP martensite (α'-Ti) phase is present in the powders. It is difficult to identify the martensitic phase from the equilibrium α phase due to the close resemblance of the two hexagonal structures. The Ti64 powder is deposited with supersonic speed at which particle interlocking and adiabatic shear bonding can form within nanoseconds. Such short exposure of the powder particles to the environment can induce neither significant atomic diffusion nor bulk phase transformation. [28, 39]. As a result of this, the coating also comprises essentially of the α' phase. On the other hand, the α and β phases were clearly revealed [40] after etching the substrate (Figure 7e). Also a clear, albeit weak, peak from the β phase is seen at ~57° in the substrate, that is absent in both the powder and coating spectra. Although, the (110)-β peak of the substrate at ~39° overlaps with the (100)-α peak, the weak (200)-β could be isolated in the spectrum; the intensity of the peak increases after aging [41, 42].

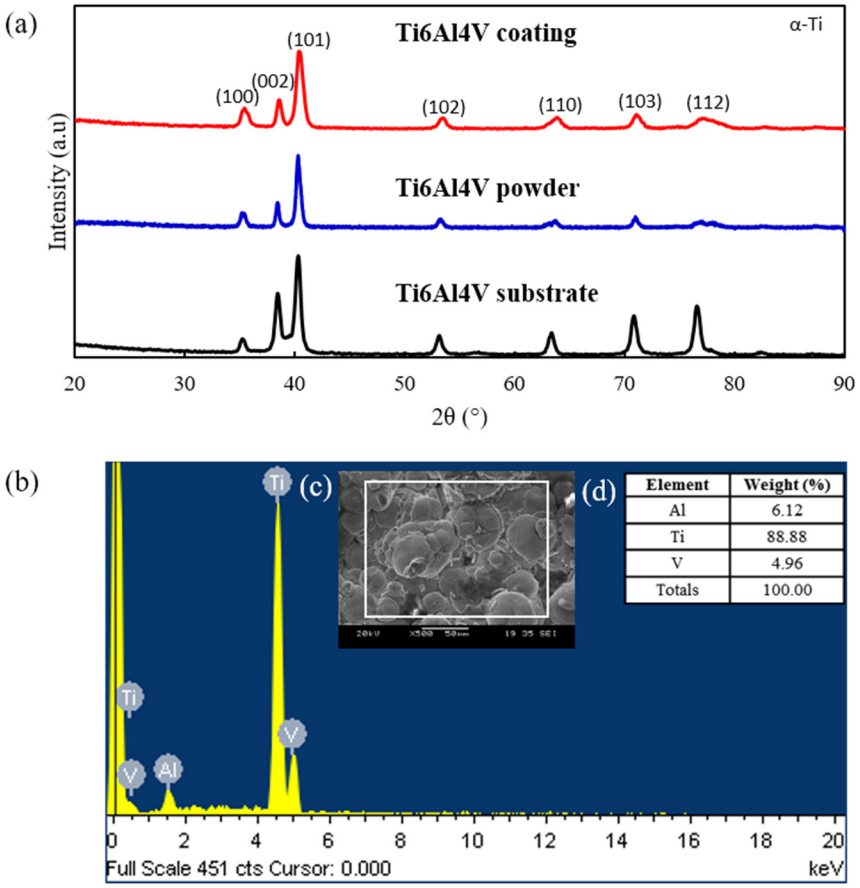

Figure 9: (a) XRD spectra of Ti64 coating, powder and substrate (referred from [43]), (b) EDS spectrum of as-sprayed 1 mm thick coating, (c) SEM micrograph of Ti64 coating where the EDS spectrum was measured and (d) elemental composition of the coating.

3.3 Hardness analysis

Figure 10a shows that the microhardness of all the Ti64 coatings is similar, around 365 - 370 HV, which exceed the hardness of the powder feedstock (3.4 ± 0.6 GPa or approx. 347.1 ± 56.1 HV) and the substrates (321.6 ± 19.1 HV), and agrees with the literature [27, 44]. This is because the particles in the coating undergo a substantial degree of work hardening as they have similar deformation as seen in Figure 7. A significantly high density of dislocations is nucleated during the impact resulting in very short mean free paths for gliding and consequently leading to strengthening via work hardening.

Nanohardness was measured across the interface of the cross-section of the 3 mm sample. The overall result in Figure 10b showed an increase in hardness near the interface which is caused by peening or hammering effect of the particles during coating build-up. The nanoidentation matrix is shown in Figure 10c. The measured coating nanohardness (4.6 ± 1 to 6.2 ± 0.5 GPa) is higher as compared to reported work on cold sprayed pure CP Ti (4 GPa) [45] due to material properties and impact velocity while the Ti64 substrate nanohardness (5.4±1 GPa) is comparable with that reported in literature [45-47]. The large error bars in the measurements are due to the sensitivity of nanohardness to the type of microstructure such as refined or parent martensitic phase in the coating corresponding to undeformed and deformed sections of the splats and the presence of the α-β dual phase structure in the substrate. The high values of nanohardness as compared to microhardness of the coating (370 HV microhardness versus 3.6 GPa nanohardness) is not surprising since metallic (or even ceramic based) materials in general are known to exhibit higher strengths at small length scales. This can be partially understood from the fact that the size of the nanoindentation within a splat is comparable to a more localised scale for example to that akin to the sub-micron grains within the deformed or individual undeformed α' lath. Thus, the large error bars in nanohardness readings is due to the stochastic distribution of defects (grain boundaries, dislocations *etc*) in highly localised areas of the coating microstructure. On the other hand, the indent size in a microhardness measurement

encompasses a larger scale of the area, compared to nanohardness, that can encompass both the deformed and undeformed sections of the splat or even a splat boundary. [48, 49].

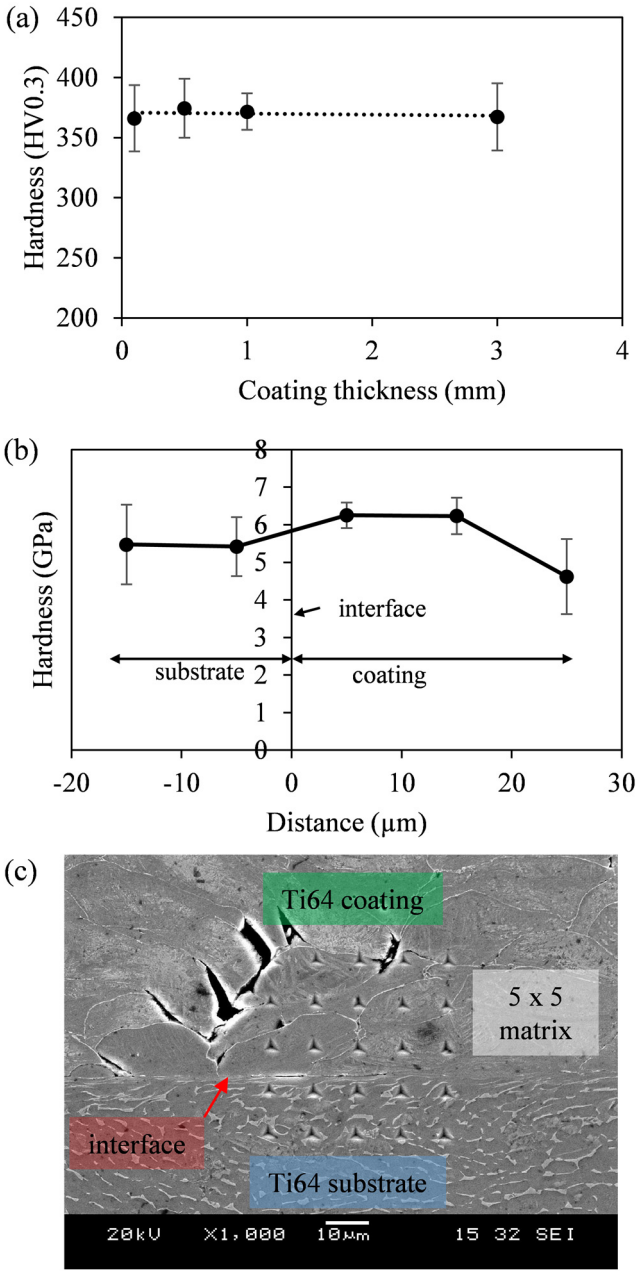

Figure 10: (a) Average hardnesses of Ti64 coated samples with different coating thicknesses and (b) nano hardnesses across the interface of 3 mm thick coating and (c) SEM micrograph of the 5x5 nanoindentation matrix.

3.4 Adhesion strength

The adhesion strength of the Ti64 coating thickness exceeded the Araldite AV170 glue strength (around 65 to 70MPa) during tensile test as shown in Figure 11, which is similar to the reported literature [25]. Analogous to thermal spray, the bond strength decreases with increasing coating thickness [20]. The adhesion strength of the coatings is mainly contributed by the adiabatic shear bonding between the impacted particles and the substrates. However, the current adhesion test standard with the ASTM C633 cannot precisely evaluate the effective bond strength of the cold sprayed Ti64 coatings to the Ti64 substrates.

Given the limitation of the above process due to glue failure, a glueless method was developed that successfully measured the true adhesion of Ti64 coating on the Ti64 substrate. The test achieved Ti64 coating/substrate interface failure at around 90 MPa, as shown in Figure 12(a-b). This method requires less amount of build-up material (that implied both cost and time saving) and machining, as compared to other techniques [50-52]. Other studies with glueless adhesion method were performed on different coating/substrate systems such as Cu/Cu, Cu/Al which has resulted in 100 to 150 MPa but suffered fractures in coating (cohesive failure) as the interface bond strength is higher than coating cohesive strength[50].

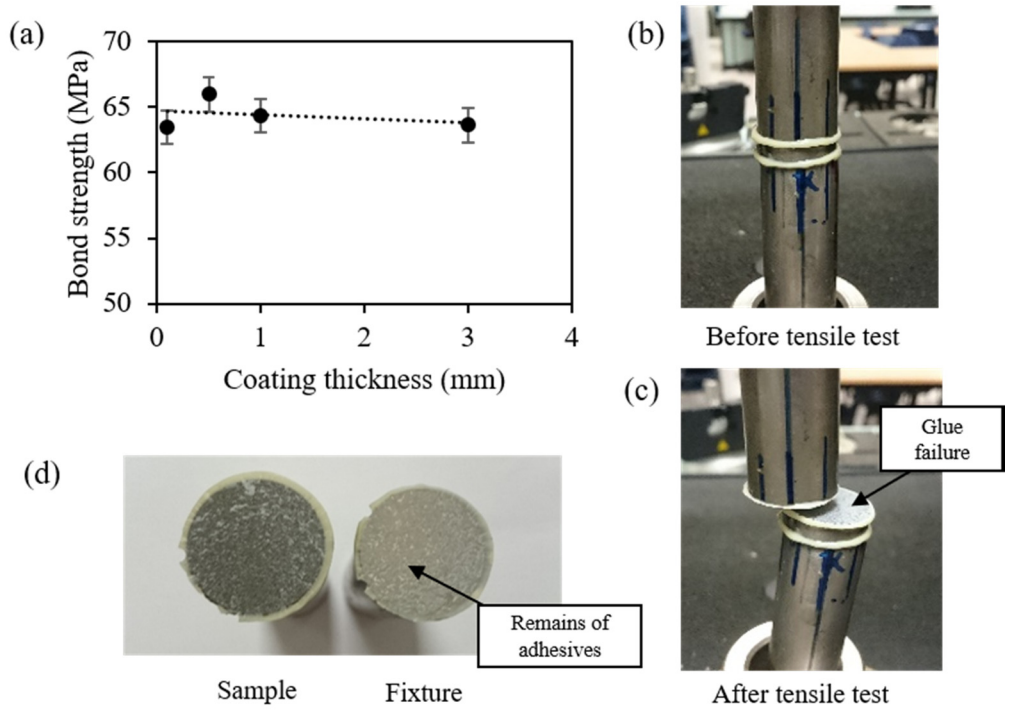

Figure 11: (a) Bond strength of Ti64 coatings as a function of coating thickness; (b) tensile test assembly before test, (c) broken test set after tensile test with glue failure and (d) photograph showing sample and fixture at glue failure with remains of adhesive.

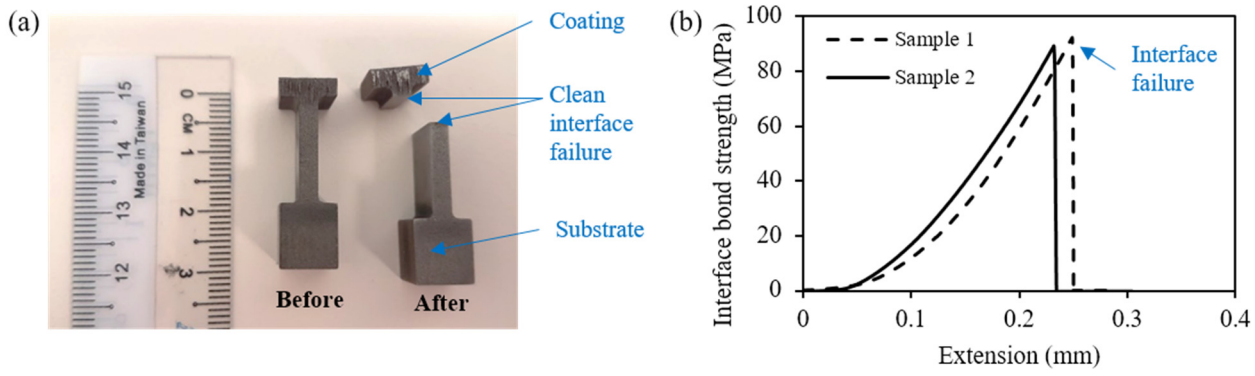

Figure 12: (a) Photographs of samples before and after tensile test where failure occurred at the substrate/coating interface and (b) interface bond strength as a function of extension

3.5 Flexural strength

Figure 13 shows the flexural stress-strain curves measured from the three-point bending tests for the Ti64 coatings with different thickness. In Figure 13a, the thinner coatings (0.1 and 0.5 mm) and the uncoated substrate show that the samples undergo (1) yielding, (2) steady plastic deformation and (3) fracture [53]. The maximum flexural stresses before failure for the uncoated substrate and the 0.1 and 0.5 mm thick coatings are 2150 (reported work for CP-Ti is 1850 MPa [54]), 1950 and 1285 MPa, respectively, corresponding to respective the flexural strains of 8.8, 5.6 and 6.3%. Figure 14 shows the fractured morphology of each sample after loading. From the top-view, the coating fracture morphologies interestingly show multiple cohesive (or interparticle) cracking in parallel to the loading axis and minor delamination from the substrates (Figure 14 (b and c)). It is also observed that the cracks in the coating did not propagate into the substrate because the cracking lines were not continuous.

The thin coatings with smaller cross-sections (coating area: 1 to 5 mm^2, depending on thickness; substrate area: 40 mm^2) than the substrates experience higher stresses during bending. The stress-strain curves for the coated samples have similar appearance as the uncoated sample (Figure 13a) – an initial elastic region is followed by a non-linear section of plastic deformation terminating to failure. The plastic region of the curves, even for the thin coating specimens, is believed to primarily arise from the strain hardening of the substrate. The yield point, the stress at which the elastic-plastic transition occurs decreases with increasing coating thickness. While the uncoated and 0.1 mm coated sample exhibit similar yield strengths, for the thicker 0.5 mm coating a much lower yield point is observed – this indicates that brittleness within the coating, rather than plasticity of the substrate, gradually becomes dominant as the coating thickness increases. This could be linked to the difference in the structure of the coating, wherein a jump in the porosity level and surface roughness is noted from 0.1 to 0.5 mm coating. Owing to tensile nature of the in-plane stresses on the surface of the coating, multiple hairline cracks start nucleating in the thin coating as shown in Figure 14(b and c). The fracture of the coatings also causes local delamination from the substrate. The out-of-plane

component of the residual stress at the coating/substrate interface in cold spraying is tensile in nature. During bend test, this residual tensile stress component acts in the same direction as the tensile component of the applied bending force, thereby assisting in delamination [55, 56].

The thicker coatings (1 and 3 mm) crack and delaminate at relatively lower flexural stresses and strains (Figure 13b). The maximum flexural stresses prior to fracture for the 1 and 3 mm thick coatings are about 550 and 519 MPa, respectively, while the flexural strains are about 0.74 and 1.2%, respectively (Figure 13b-i). Other similar work reported 500 to 750 MPa for flexural stress [57]. Also compared to the set of thin coatings, the stress-strain curves exhibit a linear response with no strain hardening – this is indicative of minimal plastic deformation within the sample and that fracture is mainly brittle. In comparison, there is no obvious indication of crack initiation in the coating before fracture as seen in the thinner coatings (Figure 14b and c). After the failure of the thicker coatings, the drop in flexural stress is then partially recovered by the substrates (Figure 13b-ii). Due to a large change of instantaneous area, the flexural stress from the rebound is not completely shown as it is artificial (flexural stresses were calculated from the original dimension). The fractured coating morphologies (Figure 14(d and e)) show that the single crack propagation is parallel to the loading direction. In addition, the Ti64 coatings also severely delaminate with a larger bending radius.

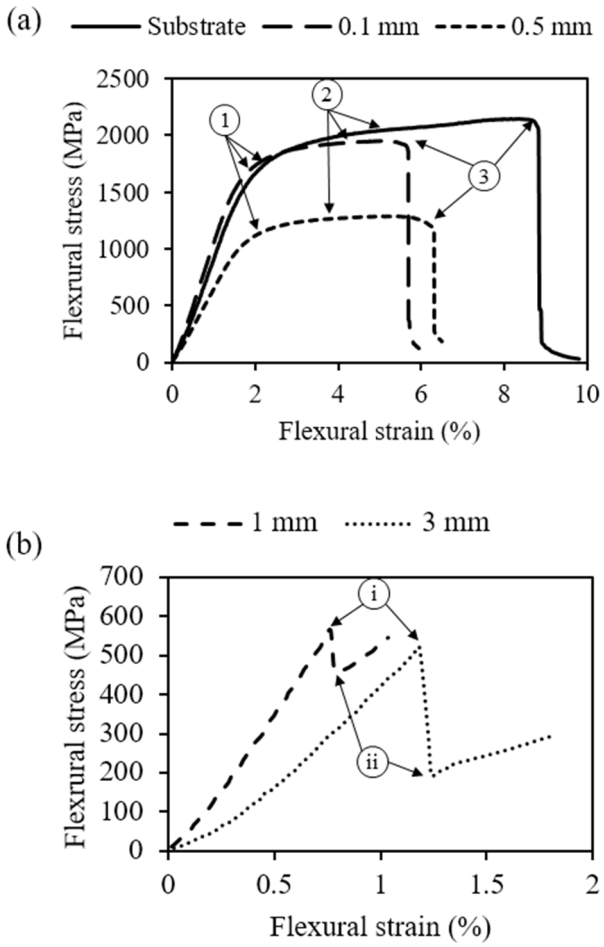

Figure 13: Stress-strain curves as a function of coating thickness: (a) bare substrate and coated samples with 0.1 mm and 0.5 mm [referred to as thinner coatings] and (b) coated samples with 1 mm and 3 mm coatings [referred to as thicker coatings].

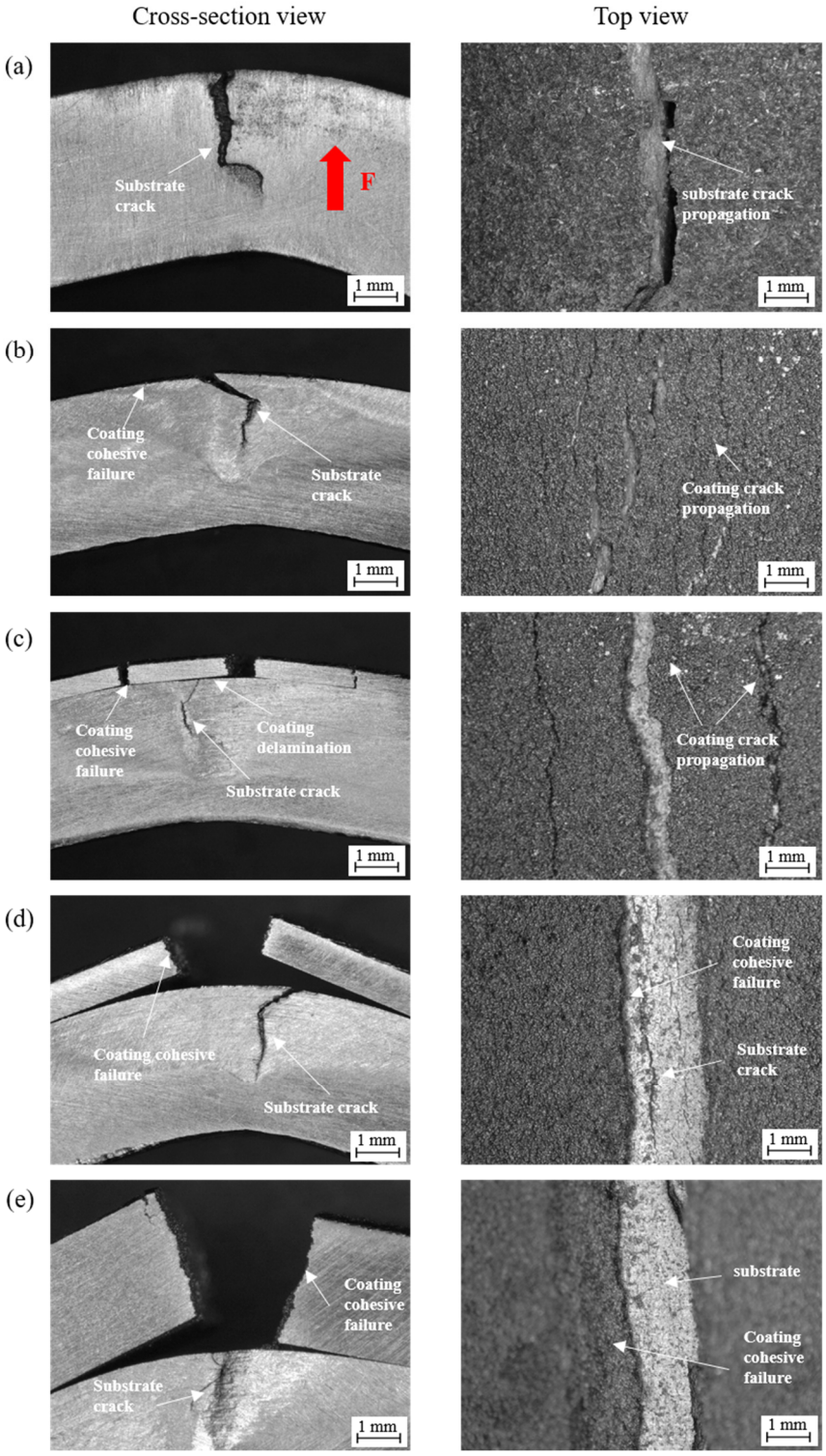

Figure 14: Side and top views of samples at crack locations after bending test: (a) bare substrate and coated samples with coating thicknesses of (b) 0.1 mm, (c) 0.5 mm, (d) 1 mm and (e) 3 mm thick. The loading direction is shown by the thick arrow.

3.6 Fractography

Figure 15 shows the etched cross sections of the selected fractured bent samples. Figure 15a shows that a crack travelled along intersplat boundaries of the coating. As the crack reaches the interface, it propagates into the substrate and/or along the coating/substrate interface (Figure 15b, c and d - circled). Due to the bending direction, the crack initiates from the coating as it experiences a higher in-plane tensile stress than the substrate. The crack is formed across the interparticle boundaries and coating/substrate interface because of weaker interfacial bond strength compared to the particles in the coating and the bulk substrate. The crack, which propagates into the substrate, initiates from the jetted region of the particle (shown within the circle in Figure 15c and d), where the actual particle bonding takes place with the flat substrate by ASI and is a region that experiences severe plastic deformation. This implies that particle debonding is a significant mechanism if coating delamination is to take place.

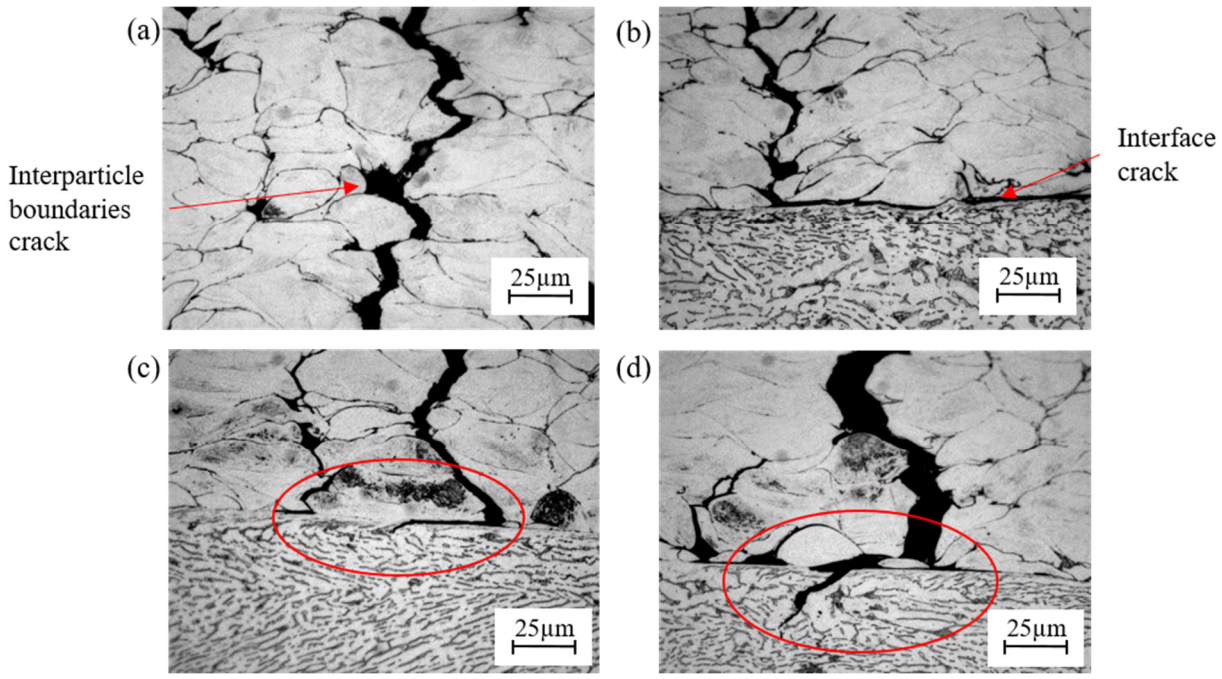

Figure 15: Fracture patterns across the cross-sections of coated samples with 0.5 mm (a and b) and 0.1 mm (c and d). The circles show that the crack initiated from particle jetted region into the substrate.

Figure 16(a and b) show the typical fractured cross-section of the Ti64 coated sample. Figure 16a (dotted square) shows a brittle fracture feature, where the particles debonded cleanly from the neighbouring particles with insignificant signs of necking due to lack of the bonding. The surfaces of the particles have dimples (Figure 16b) that are similar to the fracture patterns of the substrate shown in Figure 16(c and d), which are typical of ductile fracture behaviour. These dimple patterns belong to the fragments of the debonded Ti64 particles left adhered on the particles and are indicative of strong bonding where the particle/particle interface strength exceeds the particle cohesive strength.

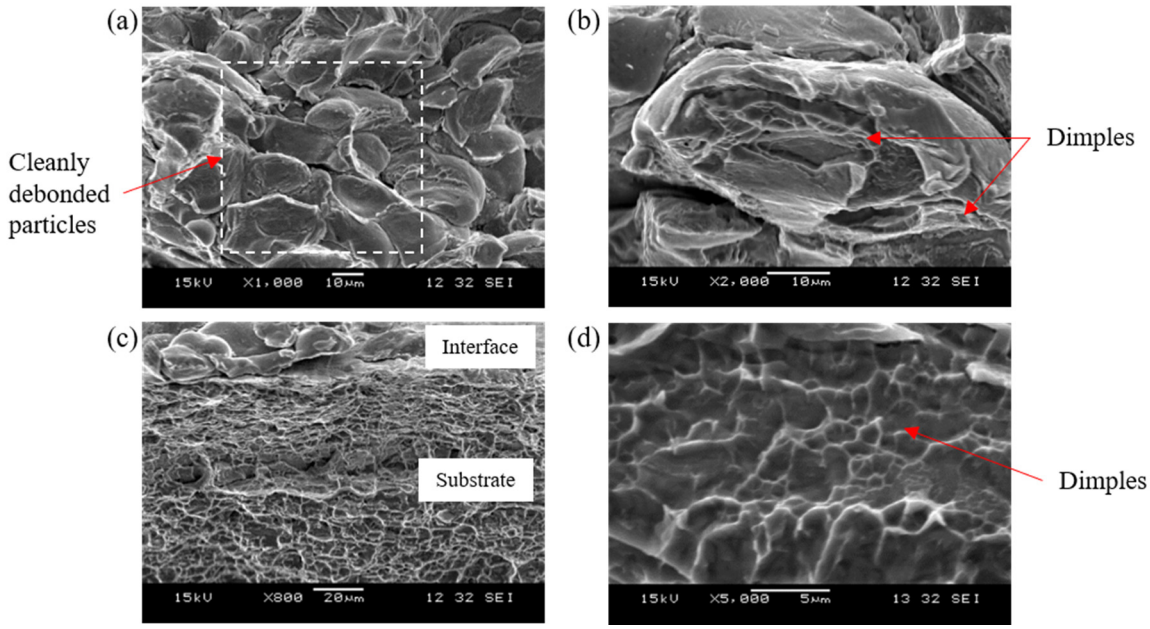

Figure 16: Fractured surface of coated sample with 3 mm thick coating (a and b) and substrate (c and d) at different magnifications

Figure 17a shows an interface fracture pattern on the coating side of the sample coated with Ti64 coating, after interface failure from the 3-point bending test. The craters are formed from the debonded particles, which remain adhered to the surface of the substrate as the particle/substrate interface bond strengths are higher than the particle/particle ones (Figure 17b). The protrusions of particles on the coating side are due to the penetration of the particles into the substrate. The particle in Figure 17c shows a smooth surface in comparison to that shown in Figure 17d, which means that no significant bonding occurs between the particles and substrate at the rim of the particles, where

extensive plastic deformation occurs. The smooth regions around the protruded particles in Figure 17a indicate no signs of bonding, which probably results due to the particles landing on the jetted region of the neighbouring particles. These observations show that bonding is not consistent, which suggest that additional heat treatment of the parent powders is required to reduce their hardness and thereby aid in improving the bonding.

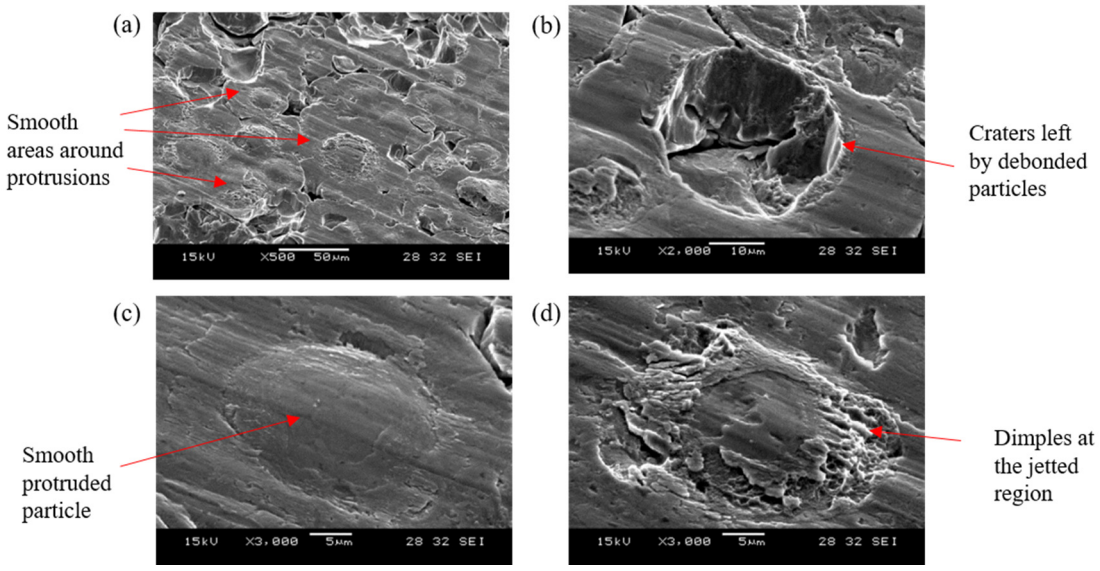

Figure 17: Interface failure on coating side of the 1 mm thick coating; (a) general view, (b) a crater formed by a fractured particle on the substrate, (c) deformed particle without bonding, and (d) fractured particle with dimples. These micrographs were taken at a tilted angle of 45°.

The interface failure on the substrate side can be observed in Figure 18a. Figure 18(b and c) shows two different crater features left by the debonded particles. Figure 18b exhibits a smoother crater with deformed rims and some debris left by the adhered particle. On the other hand, Figure 18c shows a crater with a ring of dimple fractures left by some broken pieces of the jetted section from the debonded particle (higher magnification can be observed in Figure 18d) manifesting a ductile cohesive failure as explained in the earlier section. The backscattered electron image in Figure 19a also shows that the particle/substrate boundary is well-bonded at the periphery (solid arrow) of the particle while a narrow void (dotted arrow) exists at the bottom center of the particle. When the failure happens, it is expected to have a cleaner fracture surface at the particle center than the periphery.

Figure 18e shows particles that remain bonded on the surface can withstand the tensile force because the interparticle strength is weaker as compared to the interface bond strength. Some micro-cracks are also observed at the jetted areas of the particles (Figure 18(f,-h)), which coincides with the cross-section image in Figure 15c. The impact of the particles causes substrate surface to harden due to peening effect [58] while particle deformation is accompanied with the release of heat energy close to the melting point, which may cause some localized dynamic recrystallization at the impacted area of the substrate. The bonded region of particle/substrate may be comprised of refined grains (brittle) and susceptible to crack initiation when force is applied.

Site-specific TEM foils were extracted by FIB to investigate the microstructure at the periphery of the particle where ductile cohesive fracture usually occurs in order to understand the cause of such behaviour. The bright field TEM image in Figure 19b shows the overview of the particle/substrate boundary with a good bonding which is suggested by the minimal contrast of the interface. The selected area electron diffraction pattern recorded in the circled region in Figure 19b reveals the random polycrystalline nature of the "smooth" deformed region and confirms HCP Ti within the region. Within the thin deformed band in the splat near the interface, a refined grain structure with submicron grain sizes formed by the severe refinement of the parent martensite (from initial powder) is observed [21, 45]. This nanocrystalline structure is essentially formed by rearrangement of extremely high-density dislocations into the grain boundaries. With a high internal energy imparted by supersonic particle impact to the system, the *in-situ* grain refinement is an effective way of energy minimization. In comparison, the undeformed cores (or textured regions) of the splat comprise of parent martensitic laths and the single crystal-like diffraction patterns prove that the particle/substrate boundary has crystalline HCP Ti structure, as shown in Figure 19c. Localization of strain within a thin band near the particle periphery is also a consequence of high strain rate of the particles, which is commonly observed in shock loading of metals [59, 60]. The areas of shear localization are characterized by features such as high-density shear bands, deformation twinning or dynamically recrystallized sub-micron grains.

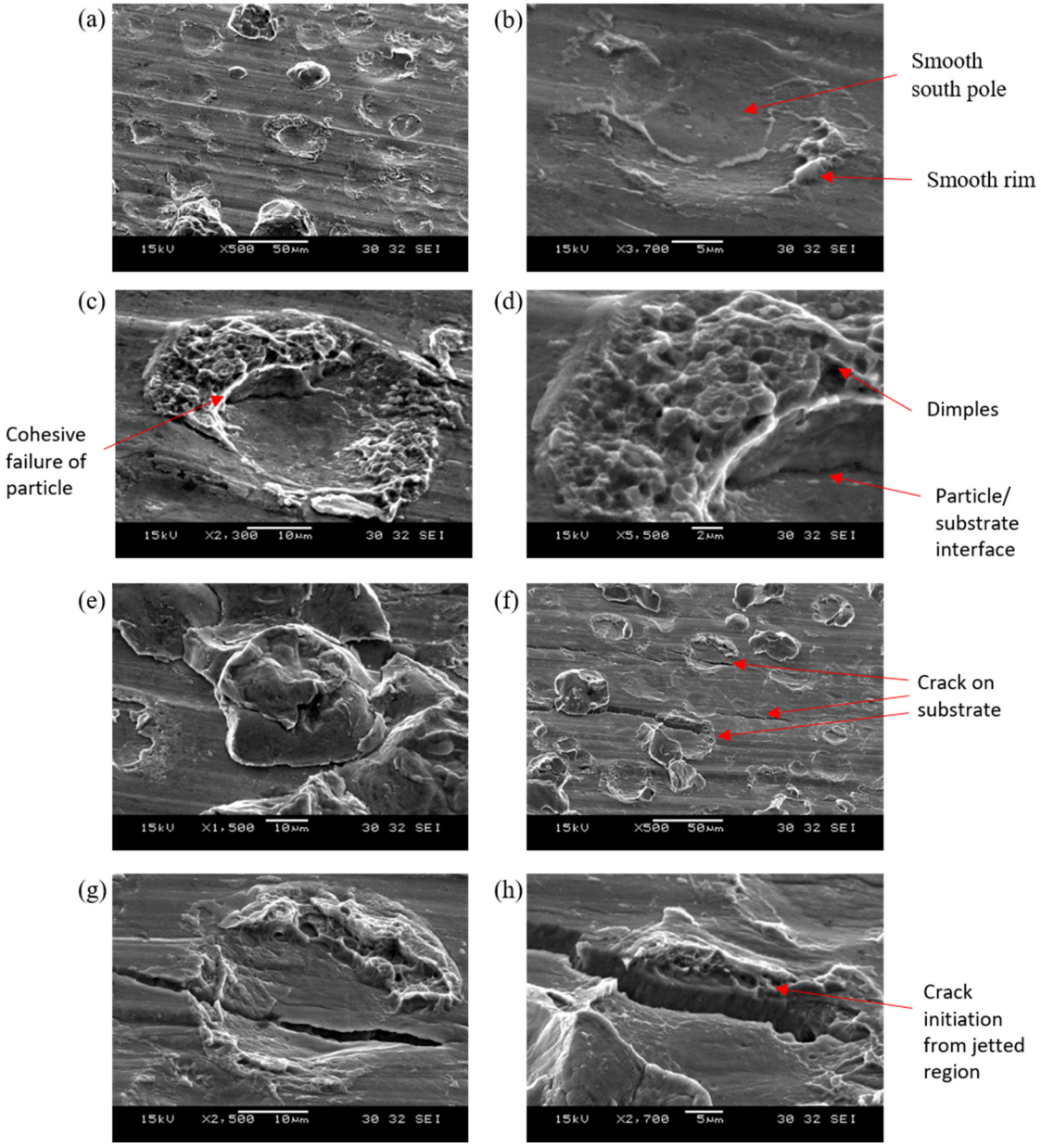

Figure 18: Interface failure on substrate side; (a) overview, (b) a crater with less dimple fracture, (c) a crater with dimple fracture, (d) a dimple fracture region, (e) particles remained on the substrate, (f) overview of cracks on substrate, and (g and h) crack at the jetted section, at different magnifications. These micrographs were taken at a tilted angle of 45°.

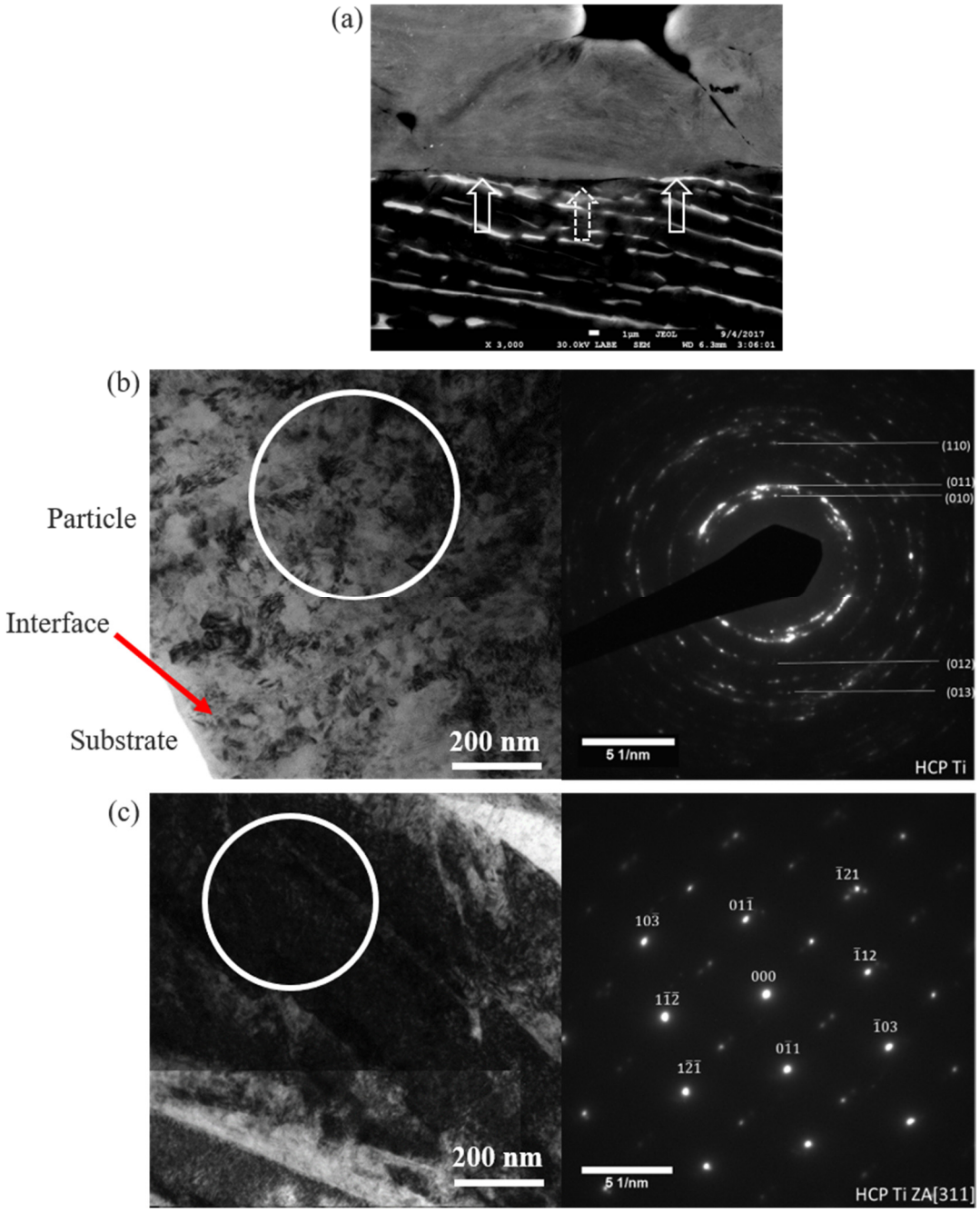

Figure 19: (a) BEI of the cross-section at the coating/substrate interface; and bright-field TEM images of (b) particle periphery near coating/substrate interface (also known as smooth region) and (c) less deformed location in coating (also known as textured region). The insets show the diffraction patterns recorded from the regions in white circles in the respective images. The solid and dotted arrows in (a) indicate the particle periphery and bottom, respectively.

4 Conclusions

The microstructure, mechanical properties and thickness effect of cold sprayed Ti64 coatings on Ti64 substrates have been studied here. The cross-section of each Ti64 coating had low porosities in the range of 2.7 to 3%. The cross-section microstructure and surface morphology also revealed no drastic change across coating thickness as most sprayed particles were severely plastically deformed and bonded via adiabatic shear instabilities. The surface roughness of the coated samples slightly increased, by about 0.1%, with coating thickness. The Ti64 coatings had an average microhardness of about 370 $HV_{0.3}$, which were consistently harder than the Ti64 powder and Ti64 substrates used in this study and due to the work-hardening of the Ti64 particles during cold spraying. The interfacial bond strength of the Ti64 coatings to their substrates exceeded 65 MPa, where the failure occurred at the adhesive glue while glueless tensile test showed even higher interface bond strengths of up to 90 MPa. The flexural strength of the Ti64 coatings decreased with increasing coating thickness due to the interparticle failure and interface delamination of the coatings from the substrates. The fractured coating/substrate interfaces following the pull-out test showed a combination of local ductile and brittle fracture. Ductile fractures corresponded to the regions of material jetting in the splats where bonding occurs, while the brittle fractures occurred in the south-pole of the splat, which have no bonding. In summary, the overall results showed that high-quality of Ti64 coatings were achieved by cold spray, even across different thicknesses, which shows good potential for repair and restoration of damaged components.

5 Acknowledgements

This work was financially supported by the National Research Foundation (NRF), Rolls-Royce (RR) and Nanyang Technological University (NTU), Singapore with the research grant (M-RT3.1: Metal Cold Spray). Authors appreciated the technical advice from Nicholas Weeks, Anna Tai and Harry

Eyre. Authors acknowledge the Facility for Analysis, Characterisation, Testing and Simulation (FACTS), NTU, Singapore, for use of their electron microscopy facilities.

References

[1] R.R. Boyer, An overview on the use of titanium in the aerospace industry, Materials Science and Engineering: A, 213 (1996) 103-114.

[2] G. Kalla, CO2-laser beam welding of structural steel with a thickness up to 20 mm, Revue de Métallurgie, 93 (1996) 1303-1310.

[3] X.-b. Wang, Temperature distribution in adiabatic shear band for ductile metal based on JOHNSON-COOK and gradient plasticity models, Transactions of Nonferrous Metals Society of China, 16 (2006) 333-338.

[4] B.S. Yilbas, M. Sami, J. Nickel, A. Coban, S.A.M. Said, Introduction into the electron beam welding of austenitic 321-type stainless steel, Journal of Materials Processing Technology, 82 (1998) 13-20.

[5] A. Papyrin, V. Kosarev, S. Klinkov, A. Alkhimov, V.M. Fomin, Cold spray technology, Elsevier2007.

[6] R.C. Dykhuizen, M.F. Smith, D.L. Gilmore, R.A. Neiser, X. Jiang, S. Sampath, Impact of high velocity cold spray particles, Journal of Thermal Spray Technology, 8 (1999) 559-564.

[7] J. Vlcek, L. Gimeno, H. Huber, E. Lugscheider, A systematic approach to material eligibility for the cold-spray process, Journal of thermal spray technology, 14 (2005) 125-133.

[8] R.C. McCune, A.N. Papyrin, J.N. Hall, W.L. Riggs, P.H. Zajchowski, An Exploration of the Cold Gas-Dynamic Spray Method for Several Materials Systems, Advances in Thermal Spray Science and Technology, DOI (1995) 1-5.

[9] V.F. Kosarev, S.V. Klinkov, A.P. Alkhimov, A.N. Papyrin, On some aspects of gas dynamics of the cold spray process, Journal of thermal spray technology, 12 (2003) 265-281.

[10] T. Schmidt, F. Gaertner, H. Kreye, New developments in cold spray based on higher gas and particle temperatures, Journal of Thermal Spray Technology, 15 (2006) 488-494.

[11] M. Grujicic, C.L. Zhao, W.S. DeRosset, D. Helfritch, Adiabatic shear instability based mechanism for particles/substrate bonding in the cold-gas dynamic-spray process, Materials & design, 25 (2004) 681-688.

[12] G. Bae, S. Kumar, S. Yoon, K. Kang, H. Na, H.J. Kim, C. Lee, Bonding features and associated mechanisms in kinetic sprayed titanium coatings, Acta Materialia, 57 (2009) 5654-5666.

[13] G. Bae, Y. Xiong, S. Kumar, K. Kang, C. Lee, General aspects of interface bonding in kinetic sprayed coatings, Acta Materialia, 56 (2008) 4858-4868.

[14] D. Goldbaum, J.M. Shockley, R.R. Chromik, A. Rezaeian, S. Yue, J.G. Legoux, E. Irissou, The Effect of Deposition Conditions on Adhesion Strength of Ti and Ti6Al4V Cold Spray Splats, Journal of Thermal Spray Technology, 21 (2011) 288-303.

[15] M.V. Vidaller, A. List, F. Gaertner, T. Klassen, S. Dosta, J.M. Guilemany, Single Impact Bonding of Cold Sprayed Ti-6Al-4V Powders on Different Substrates, Journal of Thermal Spray Technology, 24 (2015) 644-658.

[16] W.Y. Li, C. Zhang, X. Guo, J. Xu, C.J. Li, H. Liao, C. Coddet, K.A. Khor, Ti and Ti-6Al-4V Coatings by Cold Spraying and Microstructure Modification by Heat Treatment, Advanced Engineering Materials, 9 (2007) 418-423.

[17] X.T. Luo, Y.K. Wei, Y. Wang, C.J. Li, Microstructure and mechanical property of Ti and Ti6Al4V prepared by an in situ shot peening assisted cold spraying, Materials & Design, DOI 10.1016/j.matdes.2015.07.015(2015).

[18] Y. Xiong, W. Zhuang, M. Zhang, Effect of the thickness of cold sprayed aluminium alloy coating on the adhesive bond strength with an aluminium alloy substrate, Surface and Coatings Technology, 270 (2015) 259-265.

[19] A. Moridi, S.M.H. Gangaraj, S. Vezzu, M. Guagliano, Number of Passes and Thickness Effect on Mechanical Characteristics of Cold Spray Coating, Procedia Engineering, 74 (2014) 449-459.

[20] D.J. Greving, J.R. Shadley, E.F. Rybicki, D.J. Greving, J.R. Shadley, E.F. Rybicki, Effects of coating thickness and residual stresses on the bond strength of ASTM C633-79 thermal spray coating test specimens, Journal of Thermal Spray Technology, 3 (1994) 371.

[21] A.M. Birt, V.K. Champagne, R.D. Sisson, D. Apelian, Microstructural Analysis of Cold-Sprayed Ti-6Al-4V at the Micro- and Nano-Scale, Journal of Thermal Spray Technology, 24 (2015) 1277-1288.

[22] A.W.-Y. Tan, W. Sun, Y.P. Phang, M. Dai, I. Marinescu, Z. Dong, E. Liu, Effects of Traverse Scanning Speed of Spray Nozzle on the Microstructure and Mechanical Properties of Cold-Sprayed Ti6Al4V Coatings, Journal of Thermal Spray Technology, DOI 10.1007/s11666-017-0619-5(2017).

[23] ASTM International, ASTM C633-13, Standard Test Method for Adhesion or Cohesion Strength of Thermal Spray Coatings, West Conshohocken, PA, 2013.

[24] A. International, ASTM E290-14, Standard Test Methods for Bend Testing of Material for Ductility, West Conshohocken, PA,, 2014.

[25] M. Perton, S. Costil, W. Wong, D. Poirier, E. Irissou, J.G. Legoux, A. Blouin, S. Yue, Effect of Pulsed Laser Ablation and Continuous Laser Heating on the Adhesion and Cohesion of Cold Sprayed Ti-6Al-4V Coatings, Journal of Thermal Spray Technology, 21 (2012) 1322-1333.

[26] R.E. Blose, B.H. Walker, R.M. Walker, S.H. Froes, New opportunities to use cold spray process for applying additive features to titanium alloys, Metal Powder Report, 61 (2006) 30-37.

[27] P. Vo, E. Irissou, J.G. Legoux, S. Yue, Mechanical and Microstructural Characterization of Cold-Sprayed Ti-6Al-4V After Heat Treatment, Journal of Thermal Spray Technology, 22 (2013) 954-964.

[28] H. Assadi, F. Gärtner, T. Stoltenhoff, H. Kreye, Bonding mechanism in cold gas spraying, Acta Materialia, 51 (2003) 4379-4394.

[29] T.H. Van Steenkiste, J.R. Smith, R.E. Teets, Aluminum coatings via kinetic spray with relatively large powder particles, Surface and Coatings Technology, 154 (2002) 237-252.

[30] R.S. Yatnalkar, Experimental investigation of plastic deformation of ti-6al-4v under various loading conditions, The Ohio State University, 2010.

[31] T. Schmidt, F. Gärtner, H. Assadi, H. Kreye, Development of a generalized parameter window for cold spray deposition, Acta Materialia, 54 (2006) 729-742.

[32] K. Kim, M. Watanabe, J. Kawakita, S. Kuroda, Grain refinement in a single titanium powder particle impacted at high velocity, Scripta Materialia, 59 (2008) 768-771.

[33] K.H. Ko, J.O. Choi, H. Lee, Intermixing and interfacial morphology of cold-sprayed Al coatings on steel, Materials Letters, 136 (2014) 45-47.

[34] A.A. Mazilkin, G.E. Abrosimova, S.G. Protasova, B.B. Straumal, G. Schütz, S.V. Dobatkin, A.S. Bakai, Transmission electron microscopy investigation of boundaries between amorphous "grains" in Ni50Nb20Y30 alloy, Journal of Materials Science, 46 (2011) 4336-4342.

[35] B.B. Straumal, A.A. Mazilkin, B. Baretzky, Sch, uuml, G. tz, E. Rabkin, R.Z. Valiev, Accelerated Diffusion and Phase Transformations in Co–Cu Alloys Driven by the Severe Plastic Deformation, Materials Transactions, 53 (2012) 63-71.

[36] E. Irissou, J.G. Legoux, B. Arsenault, C. Moreau, Investigation of Al-Al 2O 3 cold spray coating formation and properties, Journal of Thermal Spray Technology, 16 (2007) 661-668.

[37] J. Pattison, S. Celotto, A. Khan, W. O'Neill, Standoff distance and bow shock phenomena in the Cold Spray process, Surface and Coatings Technology, 202 (2008) 1443-1454.

[38] H. Assadi, H. Kreye, F. Gärtner, T. Klassen, Cold spraying – A materials perspective, Acta Materialia, DOI 10.1016/j.actamat.2016.06.034(2016).

[39] W. Sun, A.W.Y. Tan, I. Marinescu, W.Q. Toh, E. Liu, Adhesion, tribological and corrosion properties of cold-sprayed CoCrMo and Ti6Al4V coatings on 6061-T651 Al alloy, Surface and Coatings Technology, 326 (2017) 291-298.

[40] H.K. Rafi, N.V. Karthik, H. Gong, T.L. Starr, B.E. Stucker, Microstructures and Mechanical Properties of Ti6Al4V Parts Fabricated by Selective Laser Melting and Electron Beam Melting, Journal of Materials Engineering and Performance, 22 (2013) 3872-3883.

[41] N.W. Khun, A.W.Y. Tan, W. Sun, E. Liu, Effect of Heat Treatment Temperature on Microstructure and Mechanical and Tribological Properties of Cold Sprayed Ti-6Al-4V Coatings, Tribology Transactions, DOI 10.1080/10402004.2016.1244584(2016) 1-10.

[42] L. Zeng, T.R. Bieler, Effects of working, heat treatment, and aging on microstructural evolution and crystallographic texture of α, α′, α″ and β phases in Ti–6Al–4V wire, Materials Science and Engineering: A, 392 (2005) 403-414.

[43] A.W.-Y. Tan, W. Sun, N.W. Khun, I. Marinescu, Z. Dong, E. Liu, Potential of cold spray as additive manufacturing for Ti6Al4V, Proceedings of the 2nd International Conference on Progress in Additive Manufacturing (Pro-AM 2016), Research Publishing, Singapore 2016, pp. 403-408.

[44] X.-T. Luo, Y.-K. Wei, Y. Wang, C.-J. Li, Microstructure and mechanical property of Ti and Ti6Al4V prepared by an in-situ shot peening assisted cold spraying, Materials & Design, 85 (2015) 527-533.

[45] D. Goldbaum, R.R. Chromik, N. Brodusch, R. Gauvin, Microstructure and Mechanical Properties of Ti Cold-Spray Splats Determined by Electron Channeling Contrast Imaging and Nanoindentation Mapping, Microsc Microanal, 21 (2015) 570-581.

[46] R. Li, L. Riester, T.R. Watkins, P.J. Blau, A.J. Shih, Metallurgical analysis and nanoindentation characterization of Ti–6Al–4V workpiece and chips in high-throughput drilling, Materials Science and Engineering: A, 472 (2008) 115-124.

[47] X. Gong, J. Lydon, K. Cooper, K. Chou, Microstructural Analysis and Nanoindentation Characterization of Ti-6Al-4V Parts From Electron Beam Additive Manufacturing, DOI 10.1115/IMECE2014-36675(2014) V02AT02A004.

[48] L. Qian, M. Li, Z. Zhou, H. Yang, X. Shi, Comparison of nano-indentation hardness to microhardness, Surface and Coatings Technology, 195 (2005) 264-271.

[49] H. KATO, T. Makoto, I. Kenji, Nanoindentation hardness test for estimation of vickers hardness, Transactions of JWRI, 35 (2006) 57-61.

[50] R. Huang, H. Fukanuma, Study of the Influence of Particle Velocity on Adhesive Strength of Cold Spray Deposits, Journal of Thermal Spray Technology, 21 (2011) 541-549.

[51] Y. Yuichiro, M. Shinya, Interfacial state and characteristics of cold-sprayed copper coatings on aluminum substrate, IOP Conference Series: Materials Science and Engineering, 61 (2014) 012023.

[52] R. Huang, W. Ma, H. Fukanuma, Development of ultra-strong adhesive strength coatings using cold spray, Surface and Coatings Technology, 258 (2014) 832-841.

[53] Y. Xiong, M.-X. Zhang, The effect of cold sprayed coatings on the mechanical properties of AZ91D magnesium alloys, Surface and Coatings Technology, 253 (2014) 89-95.

[54] J.A. Atoui, D.N.B. Felipucci, V.O. Pagnano, I.A. Orsi, M.A.d.A. Nobilo, O.L. Bezzon, Tensile and Flexural Strength of Commercially Pure Titanium Submitted to Laser and Tungsten Inert Gas Welds, Brazilian Dental Journal, 24 (2013) 630-634.

[55] V. Teixeira, Mechanical integrity in PVD coatings due to the presence of residual stresses, Thin Solid Films, 392 (2001) 276-281.

[56] S.J. Howard, Y.C. Tsui, T.W. Clyne, The effect of residual stresses on the debonding of coatings—I. A model for delamination at a bimaterial interface, Acta Metallurgica et Materialia, 42 (1994) 2823-2836.

[57] W. Sun, A.W.Y. Tan, N.W. Khun, I. Marinescu, E. Liu, Effect of substrate surface condition on fatigue behavior of cold sprayed Ti6Al4V coatings, Surface and Coatings Technology, DOI http://dx.doi.org/10.1016/j.surfcoat.2016.11.093(2016).

[58] A. Evans, S.B. Kim, J. Shackleton, G. Bruno, M. Preuss, P.J. Withers, Relaxation of residual stress in shot peened Udimet 720Li under high temperature isothermal fatigue, International Journal of Fatigue, 27 (2005) 1530-1534.

[59] Y.J. Chen, M.A. Meyers, V.F. Nesterenko, Spontaneous and forced shear localization in high-strain-rate deformation of tantalum, Materials Science and Engineering: A, 268 (1999) 70-82.

[60] J. Johansson, C. Persson, H. Lai, M. Hörnqvist Colliander, Microstructural examination of shear localisation during high strain rate deformation of Alloy 718, Materials Science and Engineering: A, 662 (2016) 363-372.